

# Charge-Transfer-Controlled Growth of Organic Semiconductor Crystals on Graphene

Nguyen Ngan Nguyen, Hyo Chan Lee, Min Seok Yoo, Eunho Lee, Hansol Lee, Seon Baek Lee, and Kilwon Cho\*

Controlling the growth behavior of organic semiconductors (OSCs) is essential because it determines their optoelectronic properties. In order to accomplish this, graphene templates with electronic-state tunability are used to affect the growth of OSCs by controlling the van der Waals interaction between OSC ad-molecules and graphene. However, in many graphene-molecule systems, the charge transfer between an ad-molecule and a graphene template causes another important interaction. This charge-transfer-induced interaction is never considered in the growth scheme of OSCs. Here, the effects of charge transfer on the formation of graphene-OSC heterostructures are investigated, using fullerene ( $C_{60}$ ) as a model compound. By in situ electrical doping of a graphene template to suppress the charge transfer between  $C_{60}$  ad-molecules and graphene, the layer-by-layer growth of a  $C_{60}$  film on graphene can be achieved. Under this condition, the graphene- $C_{60}$  interface is free of Fermi-level pinning; thus, barristors fabricated on the graphene- $C_{60}$  interface show a nearly ideal Schottky-Mott limit with efficient modulation of the charge-injection barrier. Moreover, the optimized  $C_{60}$  film exhibits a high field-effect electron mobility of  $2.5 \text{ cm}^2 \text{ V}^{-1} \text{ s}^{-1}$ . These results provide an efficient route to engineering highly efficient optoelectronic graphene-OSC hybrid material applications.

## 1. Introduction

Graphene has excellent properties, so the possibility of integrating it with both inorganic and organic semiconductors has been intensively studied. Graphene-semiconductor heterostructures provide multifunctionality and desirable properties for scalable and flexible optoelectronic applications.<sup>[1,2]</sup>

N. N. Nguyen, Dr. H. C. Lee, M. S. Yoo, Dr. E. Lee, H. Lee, S. B. Lee, Prof. K. Cho  
Department of Chemical Engineering  
Pohang University of Science and Technology  
Pohang 37673, Republic of Korea  
E-mail: kwcho@postech.ac.kr

 The ORCID identification number(s) for the author(s) of this article can be found under <https://doi.org/10.1002/adv.201902315>.

© 2020 The Authors. Published by WILEY-VCH Verlag GmbH & Co. KGaA, Weinheim. This is an open access article under the terms of the Creative Commons Attribution License, which permits use, distribution and reproduction in any medium, provided the original work is properly cited.

DOI: 10.1002/adv.201902315

The ideally  $sp^2$ -hybridized carbon atoms of graphene constitute a basal plane with no dangling bonds, so it provides an atomically clean interface with a semiconductor; this contact is extraordinary and cannot be achieved with traditional interfaces. With the introduction of these unique graphene-semiconductor interfaces, researchers have proposed various graphene-semiconductor hybrid optoelectronic devices such as field-effect transistors (FETs), light-emitting diodes, solar cells, photodetectors, and barristors.<sup>[3-5]</sup>

Graphene is inert and is composed of a single-atom-thick layer, so it is a useful growth template for semiconductors, especially organic semiconductors (OSCs).<sup>[6,7]</sup> The assembly of OSC thin films on graphene is mainly determined by the interactions between OSC ad-molecules and the graphene template (e.g., van der Waals). Therefore, the graphene template can enable epitaxial growth of highly crystalline OSC thin films.<sup>[8]</sup> In addition, these interactions can easily be tuned by controlling the electronic properties of graphene,<sup>[9,10]</sup> so graphene templates

offer a facile and direct approach to prepare graphene-OSC heterostructures with desirable interfacial properties. However, despite the great potential of graphene-OSC heterostructures, only a few studies of OSCs' growth behavior on electronic-states-controlled graphene have been reported.<sup>[7,10]</sup> Therefore, to develop a reliable method to optimize the growth of OSCs on graphene templates, the complex of OSC molecules and graphene templates and possible interactions between them should be investigated.

Here, we demonstrate that an epitaxial growth of a vacuum-deposited fullerene ( $C_{60}$ ) thin film on a graphene template can be controlled by tuning charge transfer between them. The Fermi level ( $E_F$ ) of the graphene template determines the amount of charge transfer between the graphene and the  $C_{60}$  ad-molecules, and this amount in turn affects the molecular dynamics of  $C_{60}$  on the graphene template. By finely tuning the  $E_F$  of the graphene template, we induced layer-by-layer growth of highly ordered  $C_{60}$  films on graphene. Considering that the thin film's topological and crystalline features determine the optoelectronic properties of OSCs,<sup>[11]</sup> this approach advances the efficiency of organic electronic devices. The  $C_{60}$  films grown

under optimized conditions exhibited a maximum field-effect mobility of  $2.5 \text{ cm}^2 \text{ V}^{-1} \text{ s}^{-1}$ . Furthermore, a graphene- $\text{C}_{60}$  Schottky junction prepared by our method approached the Schottky-Mott limit, which is desirable for highly efficient graphene-OSC barristors and other vertical graphene-OSC hybrid optoelectronic devices.

## 2. Results and Discussion

### 2.1. Charge Transfer between Graphene and $\text{C}_{60}$

We first investigated the transfer of electrons from graphene to  $\text{C}_{60}$ . Analyses using ultraviolet photoelectron spectroscopy, Kelvin probe force microscopy, and Raman spectroscopy revealed that the adsorption of  $\text{C}_{60}$  molecules induced p-type doping of graphene (Figure S2, Supporting Information). To clarify the relationship between charge transfer and the initial electronic states of graphene, we fabricated graphene field-effect transistors (G-FETs) on 300 nm thick  $\text{SiO}_2/\text{Si}$  substrates and compared the transfer characteristics of the G-FETs before and after 3 s of  $\text{C}_{60}$  deposition at a deposition rate of  $5 \times 10^{-2}$  monolayer per second ( $\text{ML s}^{-1}$ ) (Figure 1a). To eliminate the contact resistance, we used transfer-length-method measurements so that the change in graphene channel resistance ( $R_{\text{Ch}}$ ) could be solely attributed to the change in charge-carrier density ( $n_g$ ,  $n_g > 0$  for electrons and  $n_g < 0$  for holes).

After  $\text{C}_{60}$  deposition, the  $R_{\text{Ch}}$  was preserved as long as the gate voltage ( $V_G$ ) was  $< -40 \text{ V}$ . This preservation demonstrates that deposition of  $\text{C}_{60}$  did not cause degradation of graphene, and more importantly, that no charge transfer occurred between graphene and  $\text{C}_{60}$  in this range of  $V_G$ . However, at  $V_G > -40 \text{ V}$ , the  $R_{\text{Ch}}-V_G$  curve shifted to the right; this change indicates that electrons were transferred from graphene to  $\text{C}_{60}$  (Figure 1b). This shift of  $R_{\text{Ch}}-V_G$  curves when the magnitude of  $V_G$  is larger than a certain value was consistently observed with other samples from different batches (Figure S3, Supporting Information).

To calculate the number of transferred electrons ( $\Delta n_{\text{CT}} \text{ cm}^{-2}$ ) at a certain  $V_G$ , the  $R_{\text{Ch}}-V_G$  curve was fitted using the constant-mobility model.<sup>[12]</sup> Then the carrier density of bare graphene before  $\text{C}_{60}$  deposition ( $n_{g,\text{bare}}$ ) and the carrier density of graphene- $\text{C}_{60}$  after  $\text{C}_{60}$  deposition ( $n_{g,\text{C}_{60}}$ ) were each calculated at each  $V_G$  as

$$n_g = \text{sgn}(V_G - V_D) \sqrt{\left(\frac{1}{\mu e R_{\text{Ch}}} \frac{L}{W}\right)^2 - n_{\text{res}}^2} \quad (1)$$

where  $V_D$  is  $V_G$  at maximum  $R_{\text{Ch}}$ ,  $\mu$  is the carrier mobility,  $e$  is the elementary charge,  $L$  is the channel length,  $W$  is the channel width, and  $n_{\text{res}}$  is the residual carrier concentration in graphene. Then  $\Delta n_{\text{CT}}$  was calculated as  $n_{g,\text{bare}} - n_{g,\text{C}_{60}}$ . Before  $\text{C}_{60}$  deposition, the fitted values of  $\mu$  and  $n_{\text{res}}$  of the graphene transistor were  $4470 \text{ cm}^2 \text{ V}^{-1} \text{ s}^{-1}$  and  $2.3 \times 10^{12} \text{ cm}^{-2}$ , respectively.

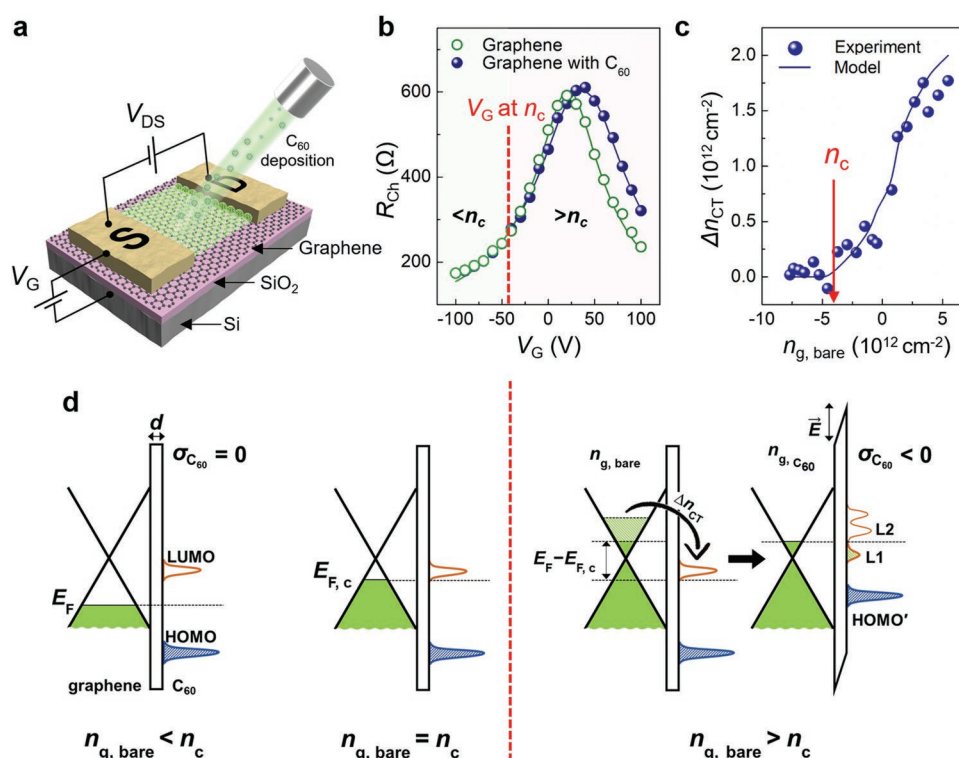


**Figure 1.** Charge transfer between graphene and  $\text{C}_{60}$ . a) Schematic diagram showing G-FET with deposited  $\text{C}_{60}$ . b) Transfer characteristic of G-FET before (green open circle) and after  $\text{C}_{60}$  deposition (blue closed circle). Solid lines are model fits. c) Concentration of transferred charge carrier after  $\text{C}_{60}$  deposition  $\Delta n_{\text{CT}}$  versus initial charge carrier concentration of bare graphene  $n_{g,\text{bare}}$ . d) Energy band diagrams of graphene/ $\text{C}_{60}$  when  $n_{g,\text{bare}} < n_c$  (left),  $n_{g,\text{bare}} = n_c$  (middle), and  $n_{g,\text{bare}} > n_c$  (right).

When plotted versus  $n_{g,bare}$  (Figure 1c), extracted  $\Delta n_{CT}$  showed no charge transfer between graphene and  $C_{60}$  when  $n_{g,bare}$  was less than a critical value,  $n_c = -4.4 \times 10^{12} \text{ cm}^{-2}$ . As  $n_{g,bare}$  approached  $n_c$ , charge transfer started and gradually increased with increasing  $n_{g,bare}$ . The  $V_G$ -dependent contact resistance in G-FETs also supports our claim that the charge transfer occurred when  $n_{g,bare} > n_c$  (Figure S4, Supporting Information).

The observed  $n_{g,bare}$ -dependent charge transfer between graphene and  $C_{60}$  is explained as follows. The electrons in graphene are transferred to  $C_{60}$  when the  $E_F$  of graphene is higher than the lowest unoccupied molecular orbital (LUMO) level of adjacent  $C_{60}$ . The LUMO level of isolated  $C_{60}$  molecules is known to be  $-4.5 \text{ eV}$ ,<sup>[13]</sup> which is similar to the  $E_F$  of undoped graphene. However, the energy levels of organic molecules change and broaden upon adsorption of  $C_{60}$ , because of the polarizability of the substrate;<sup>[14,15]</sup> thus, the LUMO level of  $C_{60}$  adsorbates can lie below the  $E_F$  of undoped graphene that has  $n_{g,bare} > n_c$ ; as a result, the graphene becomes p-type doped. The absence of charge transfer when  $n_{g,bare} < n_c$  is attributed to the  $E_F$  of graphene being lower than the LUMO level of the  $C_{60}$  adsorbates (Figure 1d, left). As the  $E_F$  of graphene is raised by external gating such that it reaches the LUMO level of  $C_{60}$ , electrons are transferred from graphene to  $C_{60}$ , and the  $E_F$  of graphene is pinned to the LUMO level of  $C_{60}$ . As a result of this charge transfer, an electric field is generated between the graphene and the  $C_{60}$ , so the vacuum level at the interface becomes tilted so that the  $E_F$  of the graphene and the LUMO level of the  $C_{60}$  are aligned (Figure 1d, right).

First, the number of charges is conserved at the graphene- $C_{60}$  interface as

$$\frac{C_g}{e}(V_G - V_{D,bare}) = n_{g,bare} = n_{g,C_{60}} + \frac{\sigma_{C_{60}}}{e} \quad (2)$$

where  $C_g$  is the dielectric capacitance,  $V_{D,bare}$  is the  $V_D$  of the G-FET before  $C_{60}$  deposition, and  $\sigma_{C_{60}}$  is the surface charge density in a  $C_{60}$  film. The charge redistribution at the graphene- $C_{60}$  interface as a function of  $n_{g,bare}$  can be estimated by solving

$$\text{sgn}(n_{g,C_{60}}) \hbar v_F \sqrt{\pi |n_{g,C_{60}}|} - \text{sgn}(n_c) \hbar v_F \sqrt{\pi |n_c|} = e \frac{\sigma_{C_{60}}}{\epsilon_0} d \quad (3)$$

where  $\hbar$  is the reduced Planck's constant,  $v_F$  is the Fermi velocity of graphene,  $\epsilon_0$  is the vacuum permittivity, and  $d$  is a fitting parameter that describes the spacing between graphene and  $C_{60}$ . The left-hand side of Equation (3) is  $E_F - E_{F,c}$  (Figure 1d), in which  $E_{F,c}$  is the critical Fermi level where the charge transfer between graphene and  $C_{60}$  occurs. The right-hand side is the charge-transfer-induced shift of the vacuum level at the interface.

The  $R_{Ch}-V_G$  curves of G-FETs and the  $\Delta n_{CT}$  as a function of  $n_{g,bare}$  were modelled using calculated  $n_{g,C_{60}}$  and  $d$ . The models successfully replicated the experimental values (Figure 1b,c). Moreover, the charge transfer modifies the density of states of  $C_{60}$  so that the LUMO level of charged  $C_{60}$  molecules is split into an "occupied" LUMO level (L1) that is shifted downward and an unoccupied LUMO level (L2) that is shifted upward (Figure 1d, right).<sup>[16]</sup> This downshift of the LUMO level upon

charge transfer can substantially stabilize  $C_{60}$  adsorbates on graphene.<sup>[17]</sup>

## 2.2. Growth of $C_{60}$ Thin Films on Graphene under Charge Transfer

With the in situ electrical gating of graphene ("Experimental and Methods" in the Supporting Information), we observed changes in i) the molecular interactions and assembly of  $C_{60}$  ad-molecules and ii) the growth behavior of  $C_{60}$  crystals as the  $E_F$  of graphene gradually approached the  $E_{F,c}$ .

First,  $C_{60}$  ad-molecules may interact with each other on the graphene surface, depending on the relative position of the  $E_F$  of graphene and the  $E_{F,c}$ . These distinctions can be well detected by Raman spectroscopy (Figure S5, Supporting Information). In both Raman spectra, the feature peaks of  $C_{60}$ , i.e., the  $A_g(1)$  mode at  $\approx 500 \text{ cm}^{-1}$  and the  $A_g(2)$  mode at  $\approx 1470 \text{ cm}^{-1}$ , were clearly observed.<sup>[18]</sup> The position of the  $A_g(2)$  peak indicates the number of intermolecular bonds to each  $C_{60}$  molecule, where each intermolecular bond shifts the peak by  $-5 \text{ cm}^{-1}$ .<sup>[19]</sup> The peak position of the  $A_g(2)$  mode of  $C_{60}$  grown on graphene with  $E_F < E_{F,c}$  is consistent with that reported for pristine  $C_{60}$  molecules.<sup>[18,19]</sup> However, the  $A_g(2)$  peak of  $C_{60}$  grown on graphene with  $E_F > E_{F,c}$  was red-shifted  $\approx 3 \text{ cm}^{-1}$ ; this change indicates that chemically bonded  $C_{60}$  dimers or oligomers were formed. This selective formation at high  $E_F$  strongly suggests that control of the  $E_F$  of graphene during  $C_{60}$  growth indeed determined the charge state of the  $C_{60}$  ad-molecules.

The charge state of  $C_{60}$  ad-molecules determines the formation of covalent bonds between two  $C_{60}$  molecules.<sup>[20,21]</sup> When  $C_{60}$  molecules have negative charges, the activation barrier for the bonding decreases. Therefore, graphene with  $E_F > E_{F,c}$  induced negative charges in  $C_{60}$  ad-molecules, resulting in the formation of intermolecular bonds between  $C_{60}$  ad-molecules. By contrast, on graphene with  $E_F < E_{F,c}$ ,  $C_{60}$  molecules were charge-neutral and thus did not form covalently bonded  $C_{60}$  dimers.

$\Delta n_{CT}$  affected molecular arrangement in  $C_{60}$  crystals, and consequently, how those crystals assembled into thin films. We used grazing incidence X-ray diffraction (GIXD) to characterize  $C_{60}$  thin films with different thicknesses grown on graphene, where  $\Delta n_{CT}$  was controlled. Under ambient conditions, the most stable structure of  $C_{60}$  crystals is face-centered cubic (fcc);<sup>[22]</sup> the diffraction patterns of the fcc  $C_{60}$  were observed in our system of  $C_{60}$  thin films grown on graphene (Figure 2a).

At the early growth stage (nominal thickness of 2.5 ML), irrespective of the occurrence of charge transfer, the set of reflections of (111) family and the reflections of plane (113) and plane (220) appeared; these reflections are located along the out-of-plane direction ( $q_z$ ) and at  $30^\circ$  and  $35^\circ$  tilt from  $q_z$ , respectively. These results indicate that  $C_{60}$  has an epitaxial relationship with graphene, with the (111) plane of  $C_{60}$  crystals parallel to the graphene substrate;<sup>[23]</sup> this epitaxy was independent of  $\Delta n_{CT}$ . However, differences were observed in the crystal domain sizes of  $C_{60}$  thin films grown on graphene at different  $\Delta n_{CT}$  (Figure 2c). We quantified the average crystal domain size of  $C_{60}$  thin films by using the Scherrer equation to estimate the domain sizes of crystal plane (111) ( $R_{(111)}$ ). When  $\Delta n_{CT} = 0$  during  $C_{60}$  growth,

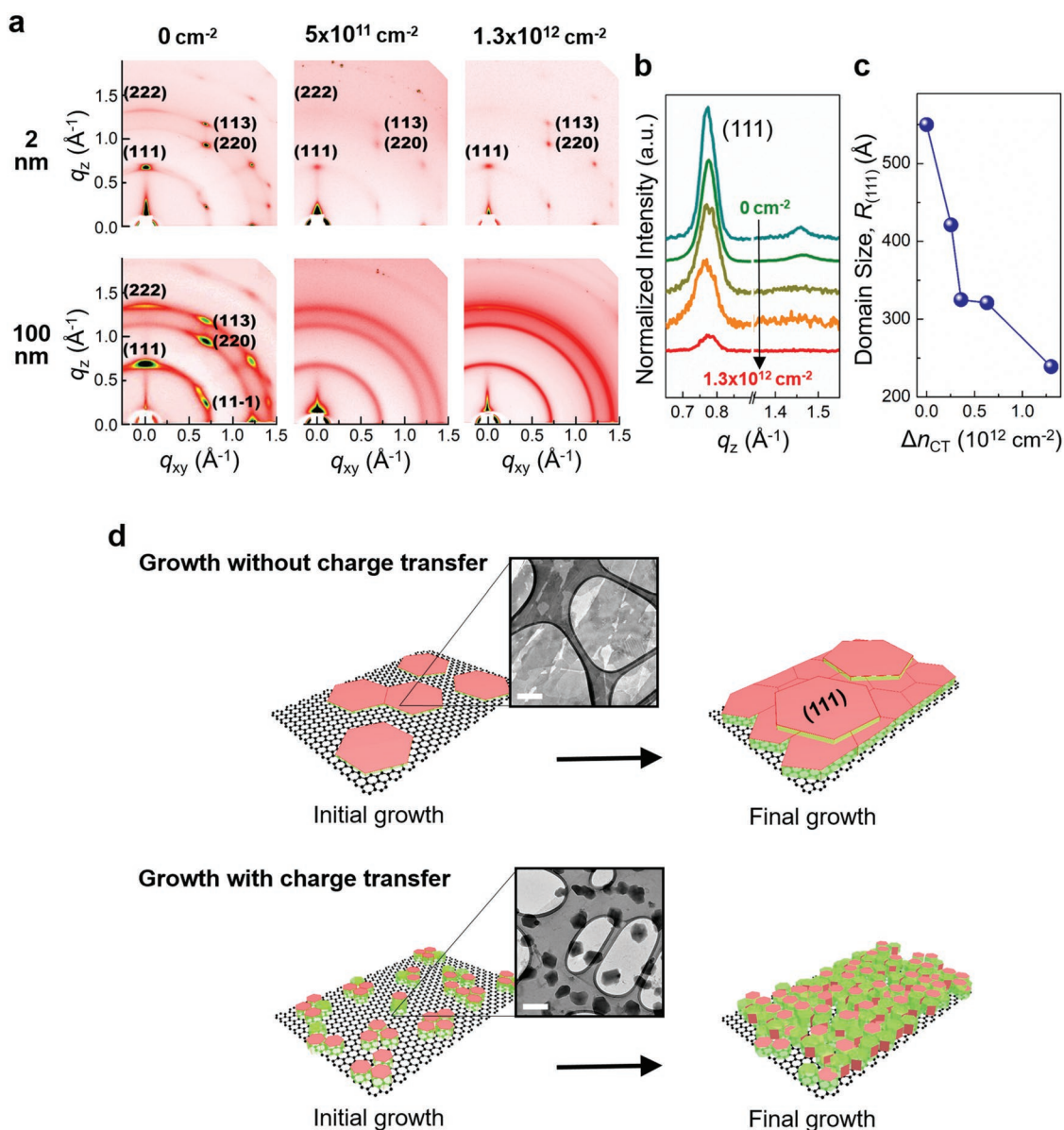


**Figure 2.** Crystal structure of C<sub>60</sub> films grown on graphene. a) 2D GIXD patterns of 2.5 ML (2 nm) and thick (100 nm) C<sub>60</sub> films grown on graphene when  $\Delta n_{CT} = 0 \text{ cm}^{-2}$  (left),  $\Delta n_{CT} = 5 \times 10^{11} \text{ cm}^{-2}$  (middle), and  $\Delta n_{CT} = 1.3 \times 10^{12} \text{ cm}^{-2}$  (right) during C<sub>60</sub> deposition. b) Cross-sectional profiles of the 2D GIXD image along the  $q_z$  for various  $\Delta n_{CT}$ . c) The mean size of the crystalline (111) domains  $R_{(111)}$  versus  $\Delta n_{CT}$ . d) Schematic illustrations of C<sub>60</sub> crystal growth on graphene without (upper) and with (lower) the charge transfer between them. Insets: Low-magnification HR-TEM images of corresponding graphene-C<sub>60</sub> samples on TEM grids. Scale bar in insets: 200 nm.

C<sub>60</sub> thin films had  $R_{(111)} \approx 60 \text{ nm}$ , which is almost three times larger than in the film grown under very high  $\Delta n_{CT}$ .

At the final growth stage, the GIXD patterns of C<sub>60</sub> films grown with and without charge transfer both showed clear ring patterns, which reveal the presence of randomly oriented C<sub>60</sub> crystals. However, the thick C<sub>60</sub> films' ordering degree was still strongly dependent on  $\Delta n_{CT}$ . On the graphene surface where  $\Delta n_{CT} = 0$ , the reflections were still sharp with a high signal-to-noise ratio, i.e., most of the C<sub>60</sub> crystals were oriented. As  $\Delta n_{CT}$  increased, these reflections weakened and eventually became undetectable; this change suggests that a large fraction of newly nucleated C<sub>60</sub> crystals were randomly oriented on the

pre-existing C<sub>60</sub> thin film. The growth behavior of C<sub>60</sub> crystals on graphene, as indicated by GIXD experiments, is summarized as follows (Figure 2d). A highly crystalline film of fcc C<sub>60</sub> was epitaxially formed on graphene via a layer-by-layer growth mode at negligible  $\Delta n_{CT}$  during C<sub>60</sub> growth. When  $\Delta n_{CT} > 0$ , despite the epitaxial relationship between graphene and C<sub>60</sub> at the early growth stage, randomly oriented nucleation occurred during vertical growth. These inferences are confirmed by low-magnification high-resolution transmission electron microscopy (HR-TEM) images (insets of Figure 2d). At  $\Delta n_{CT} = 0$ , large-area C<sub>60</sub> layers were observed; by contrast, at very high  $\Delta n_{CT}$ , small C<sub>60</sub> clusters formed. Although the GIXD results provided

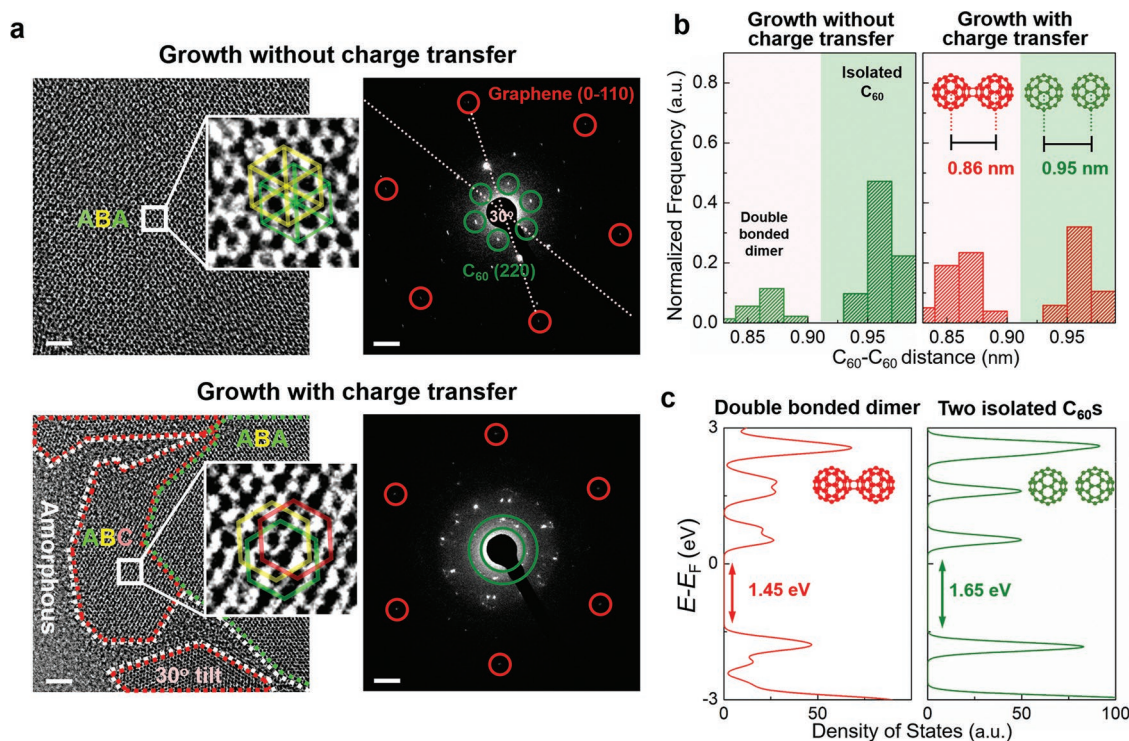


**Figure 3.** Epitaxial molecular arrangement of C<sub>60</sub> on graphene. a) Typical HR-TEM images and SAED patterns of 2.5 ML C<sub>60</sub> grown on graphene when  $\Delta n_{CT} = 0$  (top) and  $\Delta n_{CT} \gg 0$  (bottom). Scale bars in HR-TEM images: 3 nm; in SAED patterns: 1 nm<sup>-1</sup>. Insets: High-magnification HR-TEM images of regions with ABA (in top) and ABC (in bottom) stacking. b) Histogram plots of nearest neighbor C<sub>60</sub>-C<sub>60</sub> molecule distances extracted from HR-TEM images when the growth associated without (left) and with (right) charge transfer. c) DFT energetic simulations of C<sub>60</sub>-C<sub>60</sub> double-bonded dimer (left) and isolated C<sub>60</sub> molecules (right).

a hint about the crystal structure of the C<sub>60</sub> films grown on graphene over a macro area, they could not directly reveal the arrangement among C<sub>60</sub> molecules and the carbon atoms in graphene.

Therefore, C<sub>60</sub> thin films (2.5 ML) grown on graphene were imaged at high magnification using HR-TEM. The image of C<sub>60</sub> grown on graphene at  $\Delta n_{CT} = 0$  clearly showed an ordered hexagonal arrangement of C<sub>60</sub> molecules over a few tens of nanometers, which is the fashion of the (111) plane of a highly crystalline fcc structure (Figure 3a, top). Moreover, the ordering in this HR-TEM image matches that of ABA-stacked C<sub>60</sub> layers.<sup>[24]</sup> This stacking order was uniform over the analyzed areas; this consistent order implies that C<sub>60</sub> layers were preferentially stacked on each other in an ABA manner when the thin film was grown on graphene at  $\Delta n_{CT} = 0$ . The corresponding selected-area electron diffraction (SAED) pattern of this C<sub>60</sub> thin film also showed only a single set of hexagonal patterns, i.e., the crystalline orientation of C<sub>60</sub> was uniform along the vertical direction. Notably, when  $\Delta n_{CT} = 0$  was maintained during C<sub>60</sub> growth, the misorientation angles between the SAED patterns of C<sub>60</sub> and those of graphene were concentrated at close to 0° and 30°, which correspond to energetically stable adsorption sites of C<sub>60</sub> molecules along the armchair and zigzag directions of graphene, respectively (Figure S7f, Supporting Information).<sup>[23]</sup> This result is further evidence of an epitaxial relationship between graphene and C<sub>60</sub>.

By contrast, when C<sub>60</sub> was grown on graphene under a very high  $\Delta n_{CT}$ , HR-TEM image and the corresponding SAED

patterns (Figure 3a, bottom) typically revealed polycrystalline C<sub>60</sub> thin film along the lateral direction and vertical direction. This C<sub>60</sub> film showed ABA and ABC stacking mixed within small areas. In addition, small crystalline domains were tilted from the rest with a high angle ( $\approx 30^\circ$ ) in this film (Figure 3a, bottom left). Notably, the areas between the tilt grains mostly exhibited an amorphous structure. On top of this amorphous region, C<sub>60</sub> molecules could not arrange well, so the results were i) randomly oriented nucleation of C<sub>60</sub> crystals and ii) the formation of additional amorphous layers, or both. The resulting richness of tilt grain boundaries could result in the observed polycrystallinity along both the lateral and vertical directions. The dominance of (111)-plane-oriented C<sub>60</sub> crystal domains (Figure 2a) suggests the presence of an epitaxial relationship between C<sub>60</sub> and graphene at this small thickness, so grains that have high tilt angle may be formed by stitching C<sub>60</sub> domains aligned along the armchair direction and those aligned along the zigzag direction of graphene.

HR-TEM was also the best tool to investigate the chemically bonded dimers in C<sub>60</sub> films (Figure S5, Supporting Information). To quantize the dimer content, we analyzed numerous intermolecular distances of two nearest-neighbor C<sub>60</sub> molecules in films grown at  $\Delta n_{CT} = 0$  and  $\Delta n_{CT} > 0$  (Figure 3b). In both cases, the distance distribution showed peaks centered near 0.86 and 0.95 nm, but the relative peak heights depended on  $\Delta n_{CT}$ . We could assign the 0.85 nm peak to double-bonded C<sub>60</sub> dimers, and the 0.95 nm peak to isolated C<sub>60</sub> molecules.<sup>[25]</sup> When  $\Delta n_{CT} = 0$ , more than half of the intermolecular distances

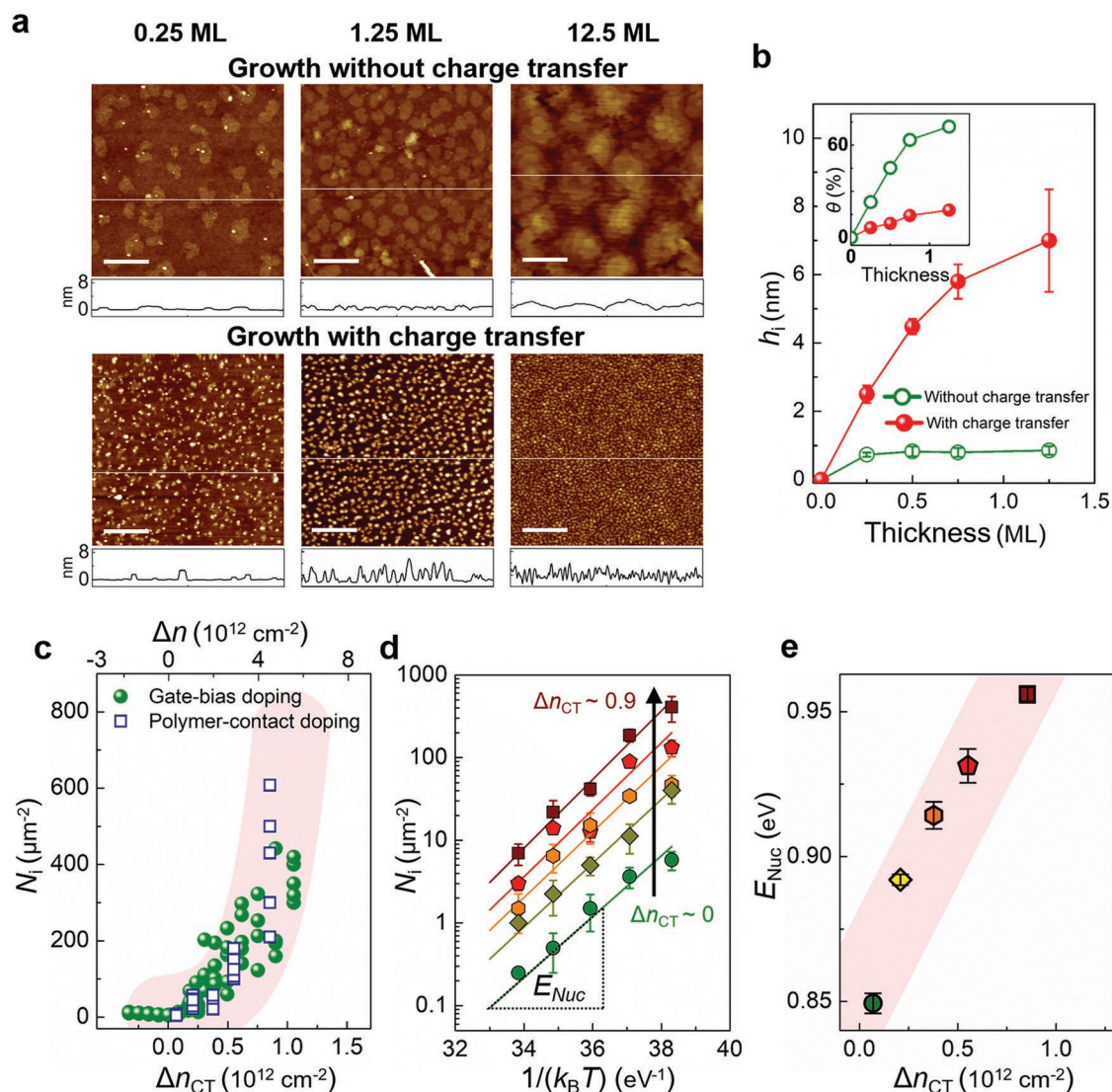


**Figure 4.** Nucleation of  $\text{C}_{60}$  islands on graphene. a) AFM images of  $\text{C}_{60}$  at different nominal thicknesses of 0.25 ML (left), 1.25 ML (middle), and 12.5 ML (right) grown on graphene, without (upper) and with (lower) the charge transfer. Scale bar: 400 nm. b) Height analysis for  $\text{C}_{60}$  islands in the AFM images. Inset: Surface coverage analysis. c) Nucleation density  $N_i$  versus  $\Delta n_{CT}$  from gate-bias (green circle) and polymer-contact doping (blue square). d)  $N_i$  versus thermal parameter  $1/(k_B T)$ . e) Nucleation energy barrier of  $\text{C}_{60}$  ( $E_{Nuc}$ ) versus  $\Delta n_{CT}$  calculated from (d). Shaded areas are to guide the eye.

were close to 0.95 nm; this consistent separation implies that a large portion of the  $\text{C}_{60}$  molecules were still free and intact. However, at  $\Delta n_{CT} > 0$  the fraction of free  $\text{C}_{60}$  molecules was substantially reduced and the proportion of double-bonded dimers increased. These results qualitatively show that charge transfer with graphene during  $\text{C}_{60}$  growth promoted the formation of double-bonded  $\text{C}_{60}$  dimers.

In addition, we performed density functional theory (DFT) simulations to calculate the electronic structure of a double-bonded  $\text{C}_{60}$  dimer and two isolated  $\text{C}_{60}$  molecules (Figure 3c; Figure S14, Supporting Information). Compared with isolated  $\text{C}_{60}$  molecules, a double-bonded  $\text{C}_{60}$  dimer showed an  $\approx 0.2$  eV smaller bandgap, and broader LUMO and highest occupied molecular orbital (HOMO) levels.

The effects of charge transfer on  $\text{C}_{60}$  growth behaviors are further demonstrated by morphological analysis using atomic

force microscopy (AFM) (Figure 4a), which enabled statistical analysis of average height  $h_i$  of  $\text{C}_{60}$  islands and surface coverage  $\theta$  of the thin films during the early growth stage (Figure 4b). On the surface of graphene templates on which charge transfer was suppressed, i.e.,  $E_F < E_{F,C}$ , the initial large-area  $\text{C}_{60}$  islands expanded laterally, to yield a constant monolayer thickness (0.8 nm) and a large increase of surface coverage. As electron transfer from the graphene to  $\text{C}_{60}$  ad-molecules increased, the number of nuclei quickly increased and each of them merely grew in height; the result was an array of grains of different heights. At  $\Delta n_{CT} = 0$ , as the growth continued, continuous  $\text{C}_{60}$  film was formed by coalescence of large-area  $\text{C}_{60}$  grains; by contrast, at  $\Delta n_{CT} > 0$ ,  $\text{C}_{60}$  film was formed by full coverage of small  $\text{C}_{60}$  islands with poor inter-grain connection. At the later growth stage (12.5 ML), the  $\text{C}_{60}$  thin film grown at  $\Delta n_{CT} = 0$  revealed clear terrace structure, which is evidence of lateral growth

mode, whereas the film grown at  $\Delta n_{CT} > 0$  simply showed an array of tiny crystallites.

The charge transfer in the graphene–C<sub>60</sub> system as well as its effects on the crystal structure and morphology of C<sub>60</sub> (Figures 2–4) were elucidated using electrically gated graphene templates. The use of polymer–substrate-doped graphene revealed similar results (Figures S1, S6, and S9, Supporting Information). This comparison emphasizes that other factors (e.g., localized traps, the wetting transparency, or contamination on the graphene surface) that might obscure the collected results might have been effectively eliminated.<sup>[7]</sup> Moreover, this polymer–substrate doping method could provide a general understanding of the observed phenomena.

To quantify the dependence of C<sub>60</sub> growth on the charge transfer from the graphene template to C<sub>60</sub> ad-molecules, numerous C<sub>60</sub> thin films with a nominal thickness of 0.25 ML were grown on graphene templates whose  $E_F$  was finely controlled by either gating or polymer–substrate doping. The plot of the nucleation density ( $N_i$ ) of these films against  $\Delta n_{CT}$  at room temperature revealed correlations between the nucleation of C<sub>60</sub> and charge transfer from graphene to C<sub>60</sub> (Figure 4c; Figure S10, Supporting Information). Clearly,  $N_i$  increased as  $\Delta n_{CT}$  increased. We also directly measured the activation energy for C<sub>60</sub> nucleation ( $E_{Nuc}$ ) as a function of  $\Delta n_{CT}$ , as  $N_i = C \exp(E_{Nuc}/(k_B T))$  where  $C$  is a pre-exponential factor,  $k_B$  is the Boltzmann constant, and  $T$  is the substrate temperature.<sup>[26]</sup> To this end,  $N_i$  values as a function of the substrate temperature  $T$  were collected at various fixed  $\Delta n_{CT}$ ; the slopes of plots of  $\ln(N_i)$  versus  $1/(k_B T)$  at a certain  $\Delta n_{CT}$  gave the values of  $E_{Nuc}$  at the  $\Delta n_{CT}$  (Figure 4d). As a result, we confirmed that  $E_{Nuc}$  increased as  $\Delta n_{CT}$  increased (Figure 4e).

### 2.3. Atomistic Mechanism of C<sub>60</sub> Thin Film Growth on Graphene under Charge Transfer

The nucleation of C<sub>60</sub> on graphene involves several atomistic processes (Figure 5a). After adsorbing to graphene, an C<sub>60</sub> ad-molecule diffuses on the surface until the molecule forms a dimer with another ad-molecule or attaches to a pre-existing island (growth).<sup>[27,28]</sup> In general,  $E_{Nuc}$  is related to the activation energies of all of these atomistic processes. However, the energy barrier for C<sub>60</sub> diffusion is negligible on graphitic surfaces,<sup>[24,29]</sup> so nucleation and growth of C<sub>60</sub> on graphene are predominantly limited by the rate of attachment of ad-molecules to pre-existing islands.

For such attachment-limited nucleation with negligible barriers to diffusion and dimerization,  $E_{Nuc} = [2E_i + 2(i + 1)E_B]/(i + 3)$ ,<sup>[27]</sup> where  $i$  is critical cluster size,  $E_i$  is cluster energy, and  $E_B$  is activation energy for the attachment.<sup>[27]</sup> This equation implies that a nucleation density increases as  $E_B$  increases. This relation is explained as follows. The presence of high  $E_B$  hinders the attachment of deposited ad-molecules to an island, so the concentration of ad-molecules increases on the graphene surface. Thus, the probability of ad-molecules colliding rapidly increases, and this change favors new nucleation rather than the growth of pre-existing islands.

Therefore, the increases in  $N_i$  and  $E_{Nuc}$  with increasing  $\Delta n_{CT}$  are attributable to the increase in  $E_B$  with increasing  $\Delta n_{CT}$  as

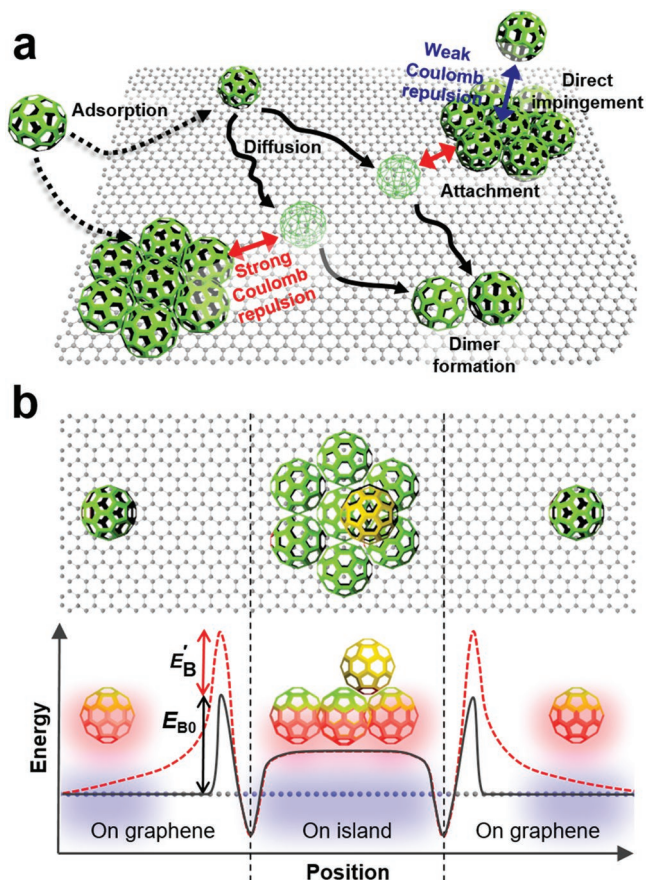


**Figure 5.** Mechanism of C<sub>60</sub> growth on graphene. a) Nucleation process of C<sub>60</sub> crystals on graphene surface that involves adsorption, diffusion, dimer formation, attachment, and direct impingement. b) Energy profiles of a C<sub>60</sub> ad-molecule versus position near and on a C<sub>60</sub> island under the absence (solid line) and presence (dashed line) of the charge transfer between the ad-molecule and graphene.

$E_B(\Delta n_{CT}) = E_{B0} + E'_B(\Delta n_{CT})$  where  $E_{B0}$  is the charge-transfer-independent attachment barrier and  $E'_B$  is the charge-transfer-dependent attachment barrier. When electrons in graphene are transferred to the ad-molecules and the islands, the ad-molecules and islands are negatively charged and the underlying graphene becomes positively charged (Figure 5b; Figure S11, Supporting Information). Consequently, repulsive Coulomb interaction occurs between the dipole from the ad-molecule–graphene and that from the island–graphene. This long-range repulsive interaction would introduce an additional attachment barrier  $E'_B$ . Assuming the long-range repulsive interaction is simple electrostatic repulsive interaction,  $E'_B$  can be estimated as

$$E'_B = Z_{avg} e^2 d \Delta n_{CT} / 2\epsilon_0 \quad (4)$$

where  $Z_{avg}$  is the average charge state of C<sub>60</sub> ad-molecules (Equation (4) is derived in the Supporting Information). This model successfully predicts the increase in  $E_B$  with increasing  $\Delta n_{CT}$ . In this argument, we assumed that repulsive Coulomb interaction between an ad-molecule and an island (and not that between two ad-molecules on graphene) dominantly affects the

nucleation kinetics. This assumption can be justified because the probability of collision between two  $C_{60}$  molecules which both simultaneously have negative charges would be very small. On the contrary, a  $C_{60}$  island contains many  $C_{60}$  molecules, so a  $C_{60}$  island is likely negatively charged.

The transition from a 2D to a 3D growth mode (Figures 2–4) under the charge transfer between graphene and  $C_{60}$  can be simply explained by invoking the repulsive Coulomb interaction between an ad-molecule and an existing island. With increasing  $\Delta n_{CT}$ ,  $E_B$  increases because of the repulsive interaction; this change inhibits the lateral growth of negatively charged islands by negatively charged ad-molecules diffusing on the graphene surface. However, irrespective of the  $E_F$  of the graphene template, the ad-molecules from the vapor phase can land directly on the top of the existing island because they are charge-neutral and thus not prone to the repulsive Coulomb interaction. However, after they are deposited on the top of the islands, their dynamics are again influenced by the  $E_F$  of graphene. When  $\Delta n_{CT} = 0$ , they can move relatively freely down to the graphene surface because the Ehrlich–Schwoebel barrier is much lower than the diffusion barrier on top of the  $C_{60}$  layer.<sup>[28]</sup> When electrons are transferred from graphene to  $C_{60}$ , the  $E_B$  increases and thus acts as an energy wall surrounding the edge of islands. For an ad-molecules on the top of the island to move downward and escape from the island, they must overcome an activation energy greater than  $E_B$ . Consequently, ad-molecules become concentrated on the top of the island, so the island rapidly grows in the vertical direction. The rapid vertical growth in turn leads to the formation of randomly oriented crystals.

#### 2.4. Charge Transport in $C_{60}$ Thin Films and Graphene– $C_{60}$ Junctions

To quantify the advantage of our growth-controlled  $C_{60}$  thin films for lateral charge transport, we grew  $C_{60}$  thin films on graphene at controlled charge-transfer conditions, then transferred the  $C_{60}$  films to octadecyltrichlorosilane (ODTS)-treated  $SiO_2/Si$  substrates and then fabricated planar  $C_{60}$  transistors ( $C_{60}$ -FETs). The final device included an  $\approx 50$  nm thick  $C_{60}$  channel without the underlying graphene (Figure 6a). We measured the transfer characteristics of  $C_{60}$ -FETs in the saturation regime with  $C_{60}$  thin-film channels grown at different  $\Delta n_{CT}$ , then estimated the associated electron field-effect mobility ( $\mu_e$ ) and measured the on/off ratio ( $I_{on}/I_{off}$ ). For a  $C_{60}$  thin film grown at  $\Delta n_{CT} = 0$ , the  $I_{on}/I_{off}$  of the FET device was  $\approx 10^7$  and the average  $\mu_e$  was  $\approx 1.5$  cm<sup>2</sup> V<sup>-1</sup> s<sup>-1</sup>. The maximum mobility of the device was  $\approx 2.5$  cm<sup>2</sup> V<sup>-1</sup> s<sup>-1</sup>, which is similar to the state-of-the-art mobility of  $C_{60}$  transistors fabricated by the vapor deposition method (Figure 6b).<sup>[5,30]</sup> With increasing  $\Delta n_{CT}$ , the  $I_{on}/I_{off}$  and  $\mu_e$  of the device substantially decreased, and eventually reached the same level of devices fabricated with polycrystalline and small-grain  $C_{60}$  (Figure 6c).<sup>[31]</sup> The decay occurs because the high  $\Delta n_{CT}$  causes low crystallinity, low uniformity and limited grain size, and these traits suppress the lateral  $\mu_e$  of  $C_{60}$  thin films.

Our method of growing  $C_{60}$  thin films on graphene provides a direct way to produce controlled graphene– $C_{60}$  van der Waals heterostructures. In addition to its use as a growth template, graphene can function as an active layer or electrode for

various flexible optoelectronic devices because of its excellent electrical conductivity and flexibility. Recently, heterostructures composed of graphene and OSCs have shown promise for use in organic photovoltaics, organic light-emitting diodes, organic photodetectors, and vertical FETs.<sup>[4,5]</sup> The electrical characteristics of such devices depend on the charge-injection efficiency at the graphene–OSC interface.

Such charge-injection efficiency at the graphene– $C_{60}$  van der Waals heterointerface formed with our method was demonstrated by fabricating two types of graphene– $C_{60}$  barristors. They had the same device structure, but one had  $C_{60}$  film grown at  $\Delta n_{CT} = 0$ , and one had  $C_{60}$  film grown at  $\Delta n_{CT} = 1 \times 10^{12}$  cm<sup>-2</sup> (Figure 6d), so the  $C_{60}$  layers had enormously different morphological and crystalline features. Both devices showed typical n-type barristor behavior (Figure 6e).<sup>[11]</sup> The closeness between the LUMO level of  $C_{60}$  and Fermi level of aluminum yields Ohmic contact between the  $C_{60}$  and the top aluminum electrode,<sup>[32]</sup> so rectifications arose from the Schottky barrier ( $\Phi_B$ ) between the  $C_{60}$  layer and the bottom graphene. Increasing the  $V_G$  barely affected the current in the forward regime ( $V_{DS} < 0$ ) but boosted the current in the reverse regime ( $V_{DS} > 0$ ). Consistent with the band diagram (Figure 1), the increase of  $V_G$  raised the Fermi level of graphene closer to the LUMO level of  $C_{60}$ , reducing the  $\Phi_B$  accordingly, until alignment was achieved between them ( $\Phi_B \approx 0$ , Ohmic contact).

Although both barristors showed rectification behavior, great distinction was observed in the current levels between the two devices. The device that used the  $C_{60}$  layer that had been grown at  $\Delta n_{CT} = 0$  showed substantial modulation of the reversed current by the gate voltage; and the on-state current  $I_{on}$  was higher in this device than in the device that used the  $C_{60}$  layer that had been grown at  $\Delta n_{CT} > 0$ , whereas their off-state currents  $I_{off}$  were similar. As a result, this device fabricated with a highly crystalline  $C_{60}$  film (i.e., grown at  $\Delta n_{CT} = 0$ ) achieved an  $I_{on}/I_{off}$  ratio of  $\approx 10^3$  at  $V_{DS} = 2$  V, which is nearly two orders of magnitude greater than the  $I_{on}/I_{off}$  ratio of the other device at the same  $V_{DS}$  (Figure 6e; Figure S12, Supporting Information).

The most important difference between the two types of barristors was the occurrence of a Schottky-to-Ohmic transition, which was only observed in the device that used the  $C_{60}$  layer that had been grown at  $\Delta n_{CT} = 0$  (Figure 6e, left). This transition occurred at  $V_G = -40$  V, which is consistent with the critical voltage ( $V_G$  at  $n_c$ ) required to induce charge transfer between graphene and  $C_{60}$  (Figure 1). By contrast, Schottky-to-Ohmic transition was not observed within the wider examining  $V_G$  range for the device with the  $C_{60}$  layer grown at  $\Delta n_{CT} > 0$  (Figure 6e, right); this absence implies that modulation of the  $E_F$  of graphene by electrical gating was limited at the graphene– $C_{60}$  interface.

Fermi-level pinning can occur when there are interfacial states in the HOMO–LUMO gap of  $C_{60}$  layers near graphene.<sup>[33]</sup> To quantitatively analyze the Fermi-level pinning, we used the diode equation in the reverse bias saturation regime,  $I_{DS} \propto T^2 \exp\left(-\frac{e\Phi_B}{k_B T}\right)$ .<sup>[11]</sup> The value of  $\Phi_B$  at each  $V_G$  was then estimated from the plot of  $\ln(I_{DS}/T^2)$  versus  $1/(k_B T)$  (Figure 6f).  $\Phi_B$  increased with increasing  $E_F$  at different rates in the two device types (Figure 6g). For the barristor with

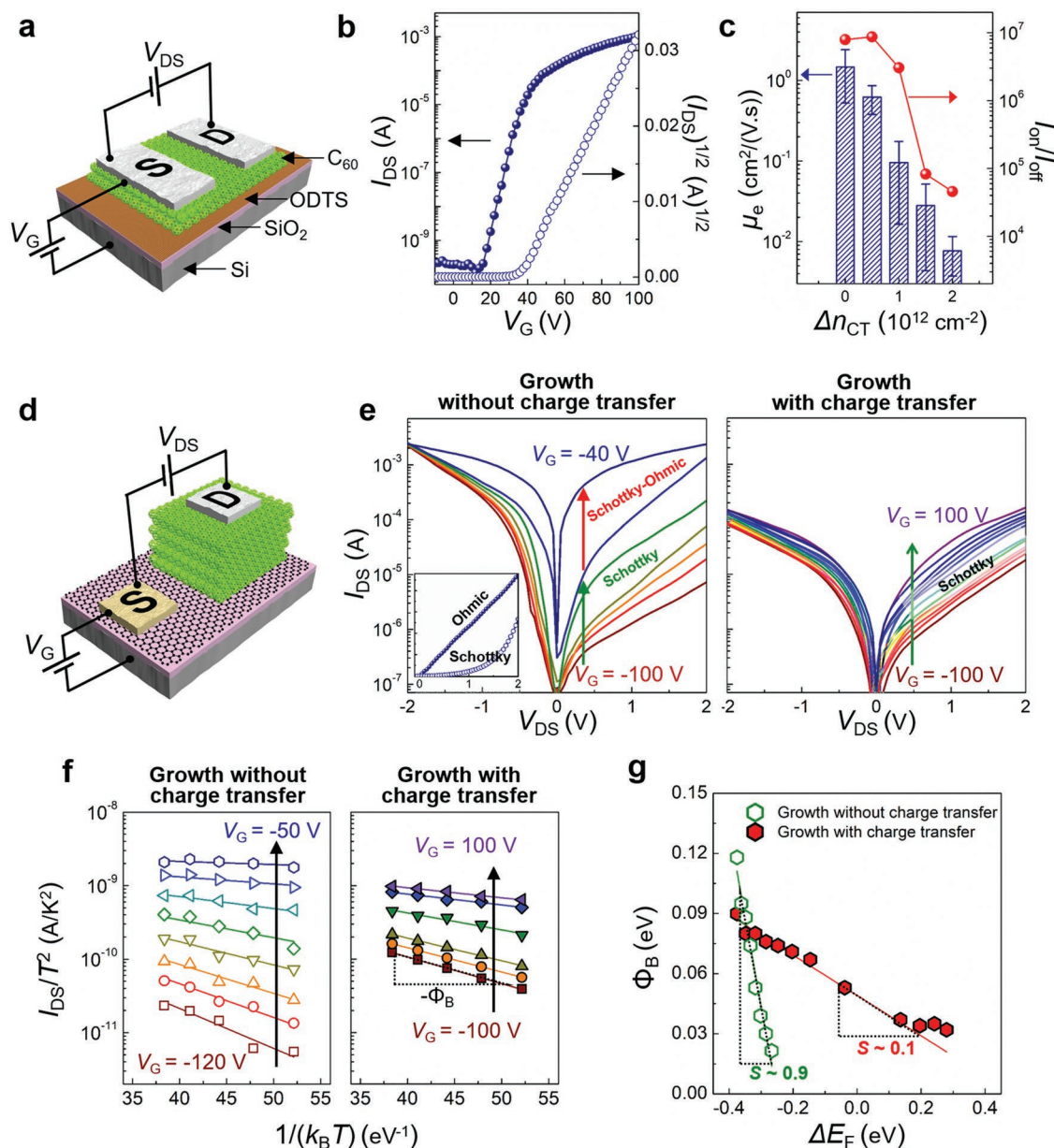


**Figure 6.** C<sub>60</sub> field-effect transistors and graphene-C<sub>60</sub> barristors. a) Schematic illustration of planar C<sub>60</sub>-FET. b) Transfer characteristic of C<sub>60</sub>-FET with C<sub>60</sub> film grown at Δn<sub>CT</sub> = 0. c) Average I<sub>on</sub>/I<sub>off</sub> and electron mobilities μ<sub>e</sub> of C<sub>60</sub>-FETs versus Δn<sub>CT</sub> during C<sub>60</sub> growth. d) Schematic illustration of graphene-C<sub>60</sub> barristor. e) I<sub>DS</sub> versus V<sub>DS</sub> of graphene-C<sub>60</sub> barristors at various fixed V<sub>G</sub> (from -100 to -40 V, step 10 V) for Δn<sub>CT</sub> = 0 (left) and at V<sub>G</sub> (from -100 to 100 V, step 10 V) for Δn<sub>CT</sub> > 0 (right). Inset: I<sub>DS</sub> versus V<sub>DS</sub> at linear scale of graphene-C<sub>60</sub> barristor for Δn<sub>CT</sub> = 0 at V<sub>G</sub> = -40 V (filled symbols) and V<sub>G</sub> = -30 V (open symbols). f) Temperature-dependent saturation current of graphene-C<sub>60</sub> barristors at various V<sub>G</sub> for Δn<sub>CT</sub> = 0 (left, step 10 V) and Δn<sub>CT</sub> > 0 cases (right, step 40 V). g) The Schottky barrier height (Φ<sub>B</sub>) obtained from (f) versus ΔE<sub>F</sub>.

the C<sub>60</sub> layer grown at Δn<sub>CT</sub> = 0, the slope  $S = d\Phi_B/dE_F$  was ≈0.9, which indicates that the graphene-C<sub>60</sub> junction in this device approached the Schottky-Mott limit.<sup>[14,34]</sup> This result demonstrates an atomically clean interface between graphene and the C<sub>60</sub> thin film, which has not been previously achieved.<sup>[23,35]</sup> To achieve this clean heterointerface for the effective tuning of the Schottky barrier, C<sub>60</sub> must be deposited directly on a thermally cleaned graphene surface,<sup>[36]</sup> and the electronic state of graphene must be optimized to effectively limit the charge transfer during growth to enable growth of

high-crystallinity C<sub>60</sub> film at the interface with graphene. The latter effect of charge transfer during the growth of OSCs has been neglected previously.

For the other device, S was only 0.1, which is indicative of strong Fermi-level pinning effect at the graphene-C<sub>60</sub> interface. The C<sub>60</sub> thin film grown on graphene with charge transfer had small and poorly connected C<sub>60</sub> grains near the graphene surface (Figures 2–4), so the interface had i) a high density of C<sub>60</sub> grain boundaries, ii) large amorphous areas, and iii) other crystalline defects that would introduce numerous interfacial trap

states (Figure S13c, Supporting Information). The Fermi level of graphene was pinned at those states. In addition, because the DFT results reveal a smaller bandgap of a C<sub>60</sub> dimer compared with two isolated C<sub>60</sub> molecules (Figure 3c), the presence of C<sub>60</sub> dimers would introduce shallow charge traps, which can further contribute to the observed Fermi-level pinning at the graphene–C<sub>60</sub> interface.

To directly confirm the interfacial states between the graphene and the C<sub>60</sub>, photocurrents of G-FETs fabricated with deposited C<sub>60</sub> thin films (20 nm) were measured under light illumination at 0.62 eV (Figure S13a, Supporting Information). For comparison, C<sub>60</sub> thin films were grown on top of graphene channels under  $\Delta n_{CT} = 0$  and  $\Delta n_{CT} > 0$ . At a high positive gate bias ( $V_G = 80$  V), only the G-FET with the C<sub>60</sub> thin film grown at  $\Delta n_{CT} > 0$  showed additional photocurrent as the device was illuminated (Figure S13b, Supporting Information). The excitation energy is much smaller than the bandgap of the C<sub>60</sub> thin film and smaller than  $2|E_F|$  of graphene at  $V_G = 80$  V, so the interband transitions are forbidden in both the C<sub>60</sub> thin film and the graphene.<sup>[37]</sup> Therefore, the photocurrent in the G-FET with a C<sub>60</sub> thin film was merely a result of detrapped electrons from the interfacial states, which were abundant in the layer grown at high  $\Delta n_{CT}$ . In fact, we observed positive photocurrent from the G-FET with the C<sub>60</sub> film grown at  $\Delta n_{CT} > 0$ , but observed no photoresponse from the device with C<sub>60</sub> film grown at  $\Delta n_{CT} = 0$ .

### 3. Conclusion

We observed that charge transfer within the graphene–C<sub>60</sub> system during the growth of C<sub>60</sub> crystals on a graphene template governed such growth and, thus governed the thin film's corresponding crystal structure and morphology. These charge-transfer phenomena altered the electronic states of the graphene–C<sub>60</sub> system, forming negatively charged C<sub>60</sub> nuclei and ad-molecules. Under these conditions, the growth of C<sub>60</sub> on graphene was favored in the vertical dimension because of the high attachment barrier energy, resulting thin films with small and randomly oriented crystallites. With this understanding, we proposed that the optimized graphene template for layer-by-layer growth of C<sub>60</sub> with large and uniformly oriented crystals is the graphene in which the charge transfer from graphene to C<sub>60</sub> is suppressed during the C<sub>60</sub> growth. Barristors fabricated with this graphene–C<sub>60</sub> van der Waals heterostructure showed efficient tunability of the charge injection barrier, approaching the Schottky–Mott limit. In addition, the lateral electron mobility  $\mu_e$  in a planar C<sub>60</sub>-FET was also boosted to a maximum  $\mu_e = 2.5$  cm<sup>2</sup> V<sup>-1</sup> s<sup>-1</sup>.

### Supporting Information

Supporting Information is available from the Wiley Online Library or from the author.

### Acknowledgements

N.N.N. and H.C.L. equally contributed to the work. This work was supported by a grant (Code No. 2011-0031628) from the Center for

Advanced Soft Electronics under the Global Frontier Research Program of the Ministry of Science and ICT, Korea. The authors thank the Pohang Accelerator Laboratory for providing the synchrotron radiation sources at 4D, 3C, and 9A beamlines used in this study.

### Conflict of Interest

The authors declare no conflict of interest.

### Keywords

charge transfer, graphene, growth template, organic electronics, organic semiconductors

Received: August 29, 2019

Revised: November 9, 2019

Published online: February 14, 2020

- [1] H. Yang, J. Heo, S. Park, H. J. Song, D. H. Seo, K. E. Byun, P. Kim, I. Yoo, H. J. Chung, K. Kim, *Science* **2012**, *336*, 1140.
- [2] a) K. Kim, J.-Y. Choi, T. Kim, S.-H. Cho, H.-J. Chung, *Nature* **2011**, *479*, 338; b) Q. H. Wang, M. C. Hersam, *Nat. Chem.* **2009**, *1*, 206; c) J. W. Colson, A. R. Woll, A. Mukherjee, M. P. Levendorf, E. L. Spitzer, V. B. Shields, M. G. Spencer, J. Park, W. R. Dichtel, *Science* **2011**, *332*, 228; d) A. Di Bartolomeo, *Phys. Rep.* **2016**, *606*, 1.
- [3] a) W. H. Lee, J. Park, S. H. Sim, S. Lim, K. S. Kim, B. H. Hong, K. Cho, *J. Am. Chem. Soc.* **2011**, *133*, 4447; b) Y. Song, X. Li, C. Mackin, X. Zhang, W. Fang, T. Palacios, H. Zhu, J. Kong, *Nano Lett.* **2015**, *15*, 2104.
- [4] a) S. B. Jo, H. H. Kim, H. Lee, B. Kang, S. Lee, M. Sim, M. Kim, W. H. Lee, K. Cho, *ACS Nano* **2015**, *9*, 8206; b) F. H. L. Koppens, T. Mueller, P. Avouris, A. C. Ferrari, M. S. Vitiello, M. Polini, *Nat. Nanotechnol.* **2014**, *9*, 780; c) T.-H. Han, Y. Lee, M.-R. Choi, S.-H. Woo, S.-H. Bae, B. H. Hong, J.-H. Ahn, T.-W. Lee, *Nat. Photonics* **2012**, *6*, 105.
- [5] C. J. Shih, R. Pfattner, Y. C. Chiu, N. Liu, T. Lei, D. Kong, Y. Kim, H. H. Chou, W. G. Bae, Z. Bao, *Nano Lett.* **2015**, *15*, 7587.
- [6] a) N. N. Nguyen, S. B. Jo, S. K. Lee, D. H. Sin, B. Kang, H. H. Kim, H. Lee, K. Cho, *Nano Lett.* **2015**, *15*, 2474; b) Y. Wang, J. A. Torres, A. Z. Stieg, S. Jiang, M. T. Yeung, Y. Rubin, S. Chaudhuri, X. Duan, R. B. Kaner, *ACS Nano* **2015**, *9*, 9486.
- [7] N. N. Nguyen, H. C. Lee, B. Kang, M. Jo, K. Cho, *Nano Lett.* **2019**, *19*, 1758.
- [8] M. Kratzer, C. Teichert, *Nanotechnology* **2016**, *27*, 292001.
- [9] a) A. Ashraf, Y. Wu, M. C. Wang, K. Yong, T. Sun, Y. Jing, R. T. Haasch, N. R. Aluru, S. Nam, *Nano Lett.* **2016**, *16*, 4708; b) G. Hong, Y. Han, T. M. Schutzius, Y. Wang, Y. Pan, M. Hu, J. Jie, C. S. Sharma, U. Muller, D. Poulikakos, *Nano Lett.* **2016**, *16*, 4447; c) C.-H. Kim, I. Kyriassis, *J. Mater. Chem. C* **2017**, *5*, 4598.
- [10] A. Kumar, K. Banerjee, M. Dvorak, F. Schulz, A. Harju, P. Rinke, P. Liljeroth, *ACS Nano* **2017**, *11*, 4960.
- [11] a) H. Sirringhaus, *Adv. Mater.* **2014**, *26*, 1319; b) T. Schuettfort, B. Watts, L. Thomsen, M. Lee, H. Sirringhaus, C. R. McNeill, *ACS Nano* **2012**, *6*, 1849; c) D. Khim, A. Luzio, G. E. Bonacchini, G. Pace, M.-J. Lee, Y.-Y. Noh, M. Caironi, *Adv. Mater.* **2018**, *30*, 1705463; d) J. Soeda, T. Okamoto, A. Hamaguchi, Y. Ikeda, H. Sato, A. Yamano, J. Takeya, *Org. Electron.* **2013**, *14*, 1211; e) T. He, Y. Wu, G. D'Avino, E. Schmidt, M. Stolte, J. Cornil, D. Beljonne, P. P. Ruden, F. Würthner, C. D. Frisbie, *Nat. Commun.* **2018**, *9*, 2141.
- [12] a) A. Venugopal, J. Chan, X. Li, C. W. Magnuson, W. P. Kirk, L. Colombo, R. S. Ruoff, E. M. Vogel, *J. Appl. Phys.* **2011**, *109*,

- 104511; b) E. Lee, H. C. Lee, S. B. Jo, H. Lee, N.-S. Lee, C. G. Park, S. K. Lee, H. H. Kim, H. Bong, K. Cho, *Adv. Funct. Mater.* **2016**, *26*, 562.
- [13] M. Gobbi, L. Pietrobon, A. Atxabal, A. Bedoya-Pinto, X. Sun, F. Golmar, R. Llopis, F. Casanova, L. E. Hueso, *Nat. Commun.* **2014**, *5*, 4161.
- [14] S. Braun, W. R. Salaneck, M. Fahlman, *Adv. Mater.* **2009**, *21*, 1450.
- [15] G. Witte, S. Lukas, P. S. Bagus, C. Wöll, *Appl. Phys. Lett.* **2005**, *87*, 263502.
- [16] C. Gaul, S. Hutsch, M. Schwarze, K. S. Schellhammer, F. Bussolotti, S. Kera, G. Cuniberti, K. Leo, F. Ortmann, *Nat. Mater.* **2018**, *17*, 439.
- [17] C. Ojeda-Aristizabal, E. J. G. Santos, S. Onishi, A. Yan, H. I. Rasool, S. Kahn, Y. Lv, D. W. Latzke, J. Velasco Jr., M. F. Crommie, M. Sorensen, K. Gotlieb, C. Y. Lin, K. Watanabe, T. Taniguchi, A. Lanzara, A. Zettl, *ACS Nano* **2017**, *11*, 4686.
- [18] V. M. Senyavin, V. A. Davydov, L. S. Kashevarova, A. V. Rakhmanina, V. Agafonov, H. Allouchi, R. Céolin, G. Sagon, H. Szwarc, *Chem. Phys. Lett.* **1999**, *313*, 421.
- [19] B. Sundqvist, *Sci. Rep.* **2015**, *4*, 6171.
- [20] Y. Zou, B. Liu, L. Wang, D. Liu, S. Yu, P. Wang, T. Wang, M. Yao, Q. Li, B. Zou, T. Cui, G. Zou, T. Wägberg, B. Sundqvist, H.-K. Mao, *Proc. Natl. Acad. Sci. USA* **2009**, *106*, 22135.
- [21] J. Fagerström, S. Stafström, *Phys. Rev. B* **1996**, *53*, 13150.
- [22] W. Zhao, W.-L. Zhou, L.-Q. Chen, Y.-Z. Huang, Z.-B. Zhang, K. K. Fung, Z.-X. Zhao, *J. Solid State Chem.* **1994**, *112*, 412.
- [23] K. Kim, T. H. Lee, E. J. G. Santos, P. S. Jo, A. Salleo, Y. Nishi, Z. Bao, *ACS Nano* **2015**, *9*, 5922.
- [24] R. Mirzayev, K. Mustonen, M. R. A. Monazam, A. Mittelberger, T. J. Pennycook, C. Mangler, T. Susi, J. Kotakoski, J. C. Meyer, *Sci. Adv.* **2017**, *3*, e1700176.
- [25] N. Kaur, K. Dharamvir, V. K. Jindal, *Chem. Phys.* **2008**, *344*, 176.
- [26] a) J. A. Venables, G. D. T. Spiller, M. Hanbucken, *Rep. Prog. Phys.* **1984**, *47*, 399; b) J. A. Venables, *Surf. Sci.* **1994**, *299–300*, 798.
- [27] J. A. Venables, H. Brune, *Phys. Rev. B* **2002**, *66*, 195404.
- [28] S. Bommel, N. Kleppmann, C. Weber, H. Spranger, P. Schafer, J. Novak, S. V. Roth, F. Schreiber, S. H. Klapp, S. Kowarik, *Nat. Commun.* **2014**, *5*, 5388.
- [29] H. Liu, P. Reinke, *J. Chem. Phys.* **2006**, *124*, 164707.
- [30] A. Virkar, S. Mannsfeld, J. H. Oh, M. F. Toney, Y. H. Tan, G. y. Liu, J. C. Scott, R. Miller, Z. Bao, *Adv. Funct. Mater.* **2009**, *19*, 1962.
- [31] a) S. Kobayashi, T. Takenobu, S. Mori, A. Fujiwara, Y. Iwasa, *Appl. Phys. Lett.* **2003**, *82*, 4581; b) R. C. Haddon, A. S. Perel, R. C. Morris, T. T. M. Palstra, A. F. Hebard, R. M. Fleming, *Appl. Phys. Lett.* **1995**, *67*, 121.
- [32] a) H. Hlaing, C. H. Kim, F. Carta, C. Y. Nam, R. A. Barton, N. Petrone, J. Hone, I. Kymissis, *Nano Lett.* **2015**, *15*, 69; b) W. Kang, M. Kitamura, Y. Arakawa, *Org. Electron.* **2013**, *14*, 644.
- [33] S. Yogeve, R. Matsubara, M. Nakamura, U. Zschieschang, H. Klauk, Y. Rosenwaks, *Phys. Rev. Lett.* **2013**, *110*, 036803.
- [34] D. Sinha, J. U. Lee, *Nano Lett.* **2014**, *14*, 4660.
- [35] a) G. Jnawali, Y. Rao, J. H. Beck, N. Petrone, I. Kymissis, J. Hone, T. F. Heinz, *ACS Nano* **2015**, *9*, 7175; b) S. Qin, X. Chen, Q. Du, Z. Nie, X. Wang, H. Lu, X. Wang, K. Liu, Y. Xu, Y. Shi, R. Zhang, F. Wang, *ACS Appl. Mater. Interfaces* **2018**, *10*, 38326.
- [36] a) Y. Liu, P. Stradins, S. H. Wei, *Angew. Chem., Int. Ed.* **2016**, *55*, 965; b) Y. Liu, P. Stradins, S.-H. Wei, *Sci. Adv.* **2016**, *2*, e1600069.
- [37] Z. Q. Li, E. A. Henriksen, Z. Jiang, Z. Hao, M. C. Martin, P. Kim, H. L. Stormer, D. N. Basov, *Nat. Phys.* **2008**, *4*, 532.